

CONTROLTAC: Force- and Position-Controlled Tactile Data Augmentation with a Single Reference Image

Dongyu Luo^{*†}, Kelin Yu^{*}, Amir-Hossein Shahidzadeh, Cornelia Fermuller,
Yiannis Aloimonos, Ruohan Gao
University of Maryland, College Park

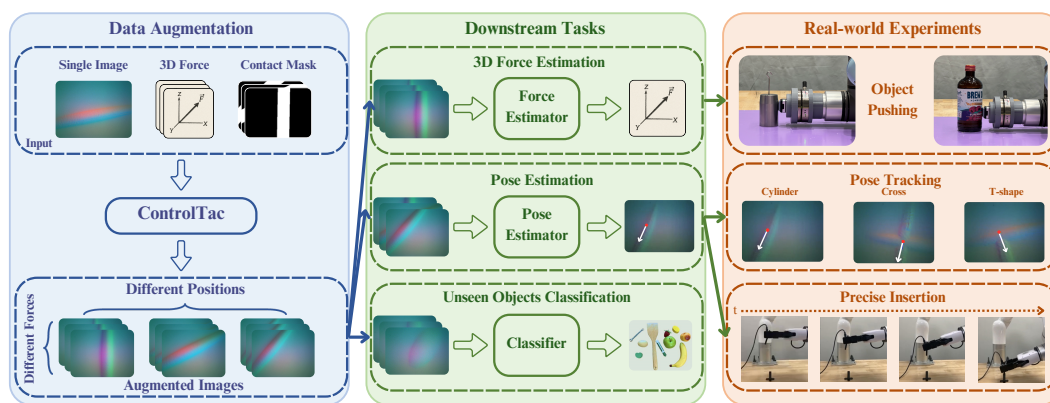


Figure 1: **Illustrations of CONTROLTAC’s utilities:** starting from a single reference image, CONTROLTAC can generate tens of thousands augmented tactile images with various contact forces and contact positions (Left). These augmented images can then be used for various downstream tasks (Middle) and deployed in three real-world experiments (Right).

Abstract

Vision-based tactile sensing has been widely used in perception, reconstruction, and robotic manipulation. However, collecting large-scale tactile data remains costly due to the localized nature of sensor-object interactions and inconsistencies across sensor instances. Existing approaches to scaling tactile data, such as simulation and free-form tactile generation, often suffer from unrealistic output and poor transferability to downstream tasks. To address this, we propose CONTROLTAC, a two-stage controllable framework that generates realistic tactile images conditioned on a single reference tactile image, contact force, and contact position. With those physical priors as control input, CONTROLTAC generates physically plausible and varied tactile images that can be used for effective data augmentation. Through experiments on three downstream tasks, we demonstrate that CONTROLTAC can effectively augment tactile datasets and lead to consistent gains. Our three real-world experiments further validate the practical utility of our approach. Project page: <https://dongyuluo.github.io/controltac>.

^{*}indicates equal contribution.

[†]Dongyu is affiliated with The University of Hong Kong. The work was done during an internship at the University of Maryland.

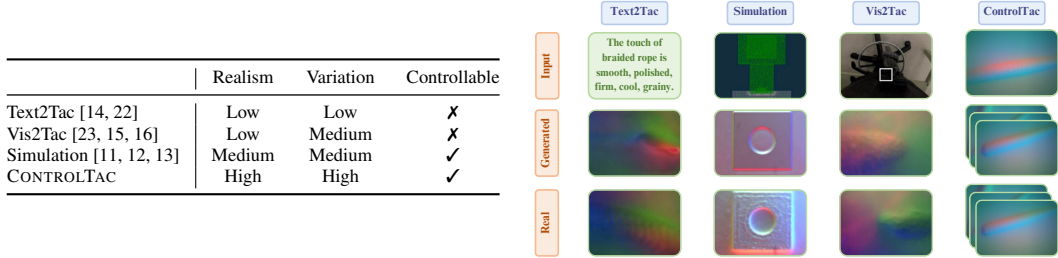


Figure 2: **Comparison of tactile data generation approaches.** We evaluate whether each method produces visually realistic images, generates varied outputs from a single input (rather than collapsing to a mean image), and allows control via physical inputs. We compare CONTROLTAC with three other directions: Text2Tactile [14, 22], Visual2Tactile [23, 16, 15], and Simulation [11, 12, 13].

1 Introduction

Vision-based tactile sensing has been widely adopted in applications such as material classification [1, 2], 3D reconstruction [3, 4, 5], and robotic manipulation [6, 7, 8]. However, collecting large-scale tactile data remains costly, as physical contact is inherently required by tactile sensing. Additionally, tactile images exhibit high variance due to differences across sensors, unstable gel properties, and varying lighting conditions, making the collected data noisy and hard to be reused by other researchers. These challenges make tactile data collection significantly more expensive than visual data, underscoring the need for efficient data augmentation methods.

Traditional data augmentation methods—such as color jittering, translation, and rotation—have also been used for tactile image classification tasks [9, 10]. However, their performance lags behind that seen in visual images, primarily due to the high variance in lighting conditions that affect tactile images. To scale up tactile datasets, two main approaches have been explored: *simulation-based methods* and *generative methods*. Simulation-based methods [11, 12, 13] aim to render tactile images by modeling sensor-object interactions. However, they often suffer from inaccurate physics and rendering inconsistencies, resulting in unrealistic outputs that diverge from real tactile observations. Generative methods, on the other hand, use both text and visual inputs to generate corresponding tactile images [14, 15, 16, 17]. While promising, these methods typically perform free-form generation without sufficient physical constraints or priors, making it difficult to produce realistic, high-fidelity tactile data. As a result, both simulation and generative methods tend to produce data that poorly match real-world tactile signals, limiting their utility to pre-training [18, 19, 20] or relative simple tasks such as contact localization [2, 16].

To generate realistic tactile images suitable for data augmentation in real-world tasks, we argue that tactile generative models must incorporate structured constraints and physical priors. Inspired by ControlNet [21], which enhances visual generation by conditioning on features such as edges and depth, we propose that tactile generation should condition on physical factors relevant to the contact—including contact force, contact location, and contact shape. These conditions are crucial for producing physically plausible tactile images that are useful for downstream tasks. In addition, conditioning on a single real tactile image provides rich structural cues—such as contact geometry and material appearance—that are difficult to obtain through direct generation or simulation, while incurring only minimal data collection overhead.

To this end, we propose CONTROLTAC, a two-stage controllable tactile generation framework that produces realistic tactile images conditioned on a single reference tactile image, contact force, and contact position. In the first stage, the model takes as input a reference tactile image with an initial contact and a relative 3D force vector to generate a target image that reflects realistic deformation and texture under the specified force. In the second stage, a ControlNet-style architecture refines the force-controlled generation by incorporating a 2D contact mask, enabling precise control over contact position. This design allows CONTROLTAC to generate a large amount of physically plausible tactile images from *just a single reference image*, leveraging different force and position inputs. Moreover, the two-stage structure enables separate modeling of priors with varying data requirements—position priors, for instance, are easier to learn with limited data. As shown in Fig. 2, our model outperforms alternatives by producing more realistic, diverse, and controllable tactile images.

We evaluate CONTROLTAC through extensive experiments and show that it generates realistic and diverse tactile images, which significantly enhance performance across multiple downstream tasks—force estimation, contact pose estimation, and object classification—and observe consistent improvements that match or even surpass models trained on substantially larger datasets. For example, in the pose estimation task, our model trained with augmented dataset can be twice as good as model trained with real data. Notably, our method can perform effective data augmentation using only a single reference image per task. In addition, we demonstrate that our model generalizes well to previously unseen objects and shapes in both pose estimations and object classification. We also deploy the trained models in real-world experiments, including a challenging task that involves precise insertion, confirming the effectiveness of our approach in dynamic real-world scenarios.

Our contributions are threefold: (1) We propose a two-stage controllable tactile generation framework for realistic tactile image generation and data augmentation; (2) We demonstrate that augmenting data with CONTROLTAC using only a single reference image significantly improves performance on three downstream tasks: force estimation, pose estimation, and object classification; (3) We successfully deploy the models trained with augmented data in real-world robot experiments, achieving strong performance on the challenging precise object insertion task.

2 Related Work

Vision-based Tactile Sensing. Recently, various tactile sensors have been used in different scenarios, such as vision-based tactile sensors [24, 25, 26, 27], magnetic tactile sensors [28, 29], and piezo-resistive tactile sensors [30, 31]. In this paper, we focus mainly on vision-based tactile sensor, which has the highest resolution and can be used to detect precise textures [1, 2] and shear forces [32, 33].

Because of its high resolution, vision-based tactile sensors have been widely utilized in different perception tasks, such as liquid property classification [34], hardness classification [35], 3D reconstruction [3, 4, 5], 3D generation [36, 37], slip detection [38], and pose estimation [3]. Also, it has been used for various robotic tasks, such as grasping [39, 40, 41], insertion [8, 7, 6], pouring [7], in-hand rotation [42], and dense packing [8, 43, 44]. However, the lack of data remains a major challenge for vision-based tactile sensing because collecting local contact on diverse objects is expensive. In this paper, we introduce a new framework for scaling up tactile datasets in downstream tasks with conditional tactile generation.

Building Tactile Datasets. To address the scarcity of tactile data, many prior works focus on collecting large-scale real-world datasets [17, 16, 45, 23]. While these efforts help scale up tactile data, the quantity remains limited, and the resulting datasets are often difficult to reuse for downstream tasks—especially in robotics tasks—due to significant variability across sensors.

Another approach is to use simulation [11, 12, 13, 46, 47], which have been widely adopted for pre-training [18, 19, 20, 48] and Sim2Real transfer [49, 46, 13]. However, bridging the Sim2Real gap remains a major challenge, as illustrated in Fig. 4. High-quality Sim2Real transfer typically still requires large real datasets for co-training [11] or the use of generative models for domain adaptation [49]. To this end, we propose a controllable tactile generation model that can scale existing tactile datasets under different physical conditions.

Tactile Image Generation. Text-to-tactile generation [14, 22] and vision-to-tactile generation [23, 16, 17, 15, 50] have been widely used for representation learning [48, 18], contact localization [16, 2], classification [16, 15], and retrieval [2, 22]. Cross-sensor generation [51] has also been explored to utilize various properties of different tactile sensors. However, as shown in Fig. 2, the free-form generation from visual images often yields low-quality outputs, limiting its utility in more complex downstream tasks. To address this, we propose a conditional diffusion model that generates tactile images for data augmentation, guided by physical constraints and priors. We present both analysis and qualitative examples in Fig. 2 to highlight the limitations of existing approaches and the strengths of our method.

Conditional Image Generation. Conditional image generation has become a central topic in generative modeling, where the goal is to generate images guided by structured inputs such as class labels, text, or physical parameters. Early methods [52, 53, 54, 55, 56, 57] based on conditional GANs [58] and conditional VAEs [59] demonstrate the feasibility of conditioning image generation on external inputs but often suffer from limitations in image quality and training stability [60, 61,

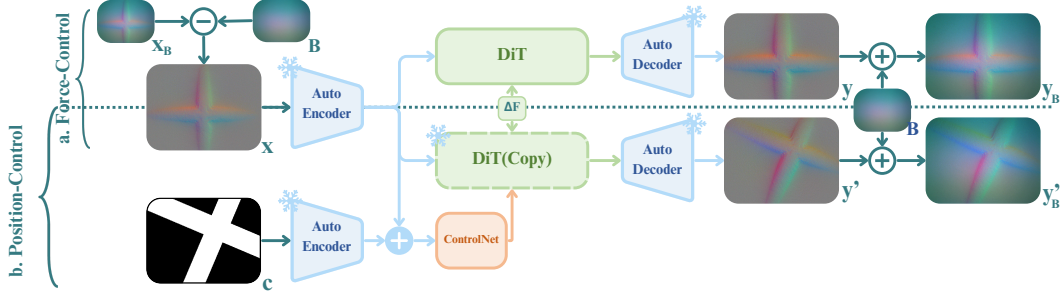


Figure 3: **Illustration of our controllable tactile generation framework.** a) The Force-Control component of CONTROLTAC. We input the tactile image x without background B into the DiT, which is conditioned on the 3D force ΔF . b) The Position-Control component of CONTROLTAC. We copy the DiT from the first stage and finetune it with ControlNet conditioned on the contact mask c for generating realistic tactile image y_B conditioned on different force and contact positions.

62, 63]. More recently, diffusion models [64, 65, 66, 67, 68, 69, 70] have emerged as state-of-the-art approaches due to their ability to generate high-fidelity and diverse images through a gradual denoising process. Meanwhile, ControlNet [21] enhances diffusion-based models by incorporating an auxiliary network that injects explicit structural conditions—such as edge maps, depth maps, or human poses—into the generation pipeline. This allows for fine-grained control over the output while maintaining the quality and diversity of diffusion models. Inspired by, but distinct from the prior work above, we tackle the new problem of controllable tactile image generation.

3 Methodology

We present CONTROLTAC, a controllable framework for generating realistic tactile images to scale up tactile dataset in downstream tasks, using only a single reference tactile image along with contact force and contact position. The key innovation lies in leveraging the reference tactile image to preserve contact texture and color, while incorporating physical conditions—force and contact location—through a two-stage conditional tactile generation pipeline. This design ensures the generated tactile images are both realistic and physically consistent, enabling effective tactile data augmentation.

In this section, we first introduce the architecture of our two-stage conditional tactile generation framework, which includes a force-control generator and a position-control generator (Sec. 3.1). Then, we demonstrate how to effectively leverage the generated data for downstream tasks such as force estimation, contact pose estimation, and object classification (Sec. 3.2). The overall architecture of our framework is illustrated in Fig. 3.

3.1 Two-stage Conditional Tactile Generation Framework

We propose a two-stage conditional tactile image generation framework that incorporates force and contact position as controllable physical priors. The model also leverages a reference tactile image to preserve color and texture cues. (1) In the first stage, the force-control generator takes a reference tactile image and the relative force as input to generate a target image that reflects the desired force. (2) In the second stage, we fine-tune the pretrained force-control generator with contact masks using ControlNet [21] to control the contact position of generated tactile images.

Force-Control Generation. To generate a tactile image corresponding to a target force, we train a conditional diffusion model defined as $y = \mathcal{D}(\mathcal{F}_f(z^{(x)}), \Delta F)$, where the Diffusion Transformer (DiT) [71] is used as the backbone and DDIM [65] serves as the sampler to improve both generation quality and inference efficiency. In this formulation, the force-control generator is denoted by $\mathcal{F}_f(\cdot)$. The target tactile image is represented by $y \in \mathbb{R}^{W \times H \times 3}$, while the reference tactile image is denoted as $x \in \mathbb{R}^{W \times H \times 3}$. The latent representation $z^{(x)} = \mathcal{E}(x)$ is obtained by encoding x using the frozen pretrained encoder $\mathcal{E}(\cdot)$ introduced in SANA [69]. The output of the diffusion model is subsequently decoded using the corresponding frozen pretrained decoder $\mathcal{D}(\cdot)$, also proposed in SANA [69]. The model is conditioned on a relative force vector $\Delta F \in \mathbb{R}^3$, computed as the difference between the desired target force F_t and the initial force F_i associated with the reference image: $\Delta F = F_t - F_i$. To

enable force-guided generation, we train the force-control generator $\mathcal{F}_f(\cdot)$ using the dataset proposed in FeelAnyForce [33], which provides ground-truth annotations of 3D force vectors.

Position-Control Mask. Before introducing the position-control generator, we first describe how the position-control signal is represented. We propose an efficient and compact representation: the contact mask. This binary mask marks the approximate contact area between object and sensor. Importantly, for a given object, the shape of the contact mask remains consistent, regardless of the applied force since we get it from the reference image with initial contact. Examples are shown in Fig. 4. Then, the variations of contact position are captured by translating and rotating the mask. To ensure accuracy, each contact mask is manually aligned with the reference tactile image, with a translation precision of one pixel and a rotation precision of one degree. This approach avoids several common challenges in defining contact position: (1) it avoids the ambiguity of representing contact using a center point (x, y) and a rotation angle, which becomes unreliable when the object is larger than the sensor’s size; (2) it avoids the inconsistency of edge detection methods such as Canny [72], which can yield different contact boundaries depending on the pressing region.

Position-Control Generation. Building upon the pretrained force-control generator $\mathcal{F}_f(\cdot)$, we utilize the ControlNet [21] to fine-tune the force-control generator using the contact mask as a control signal. Specifically, we follow the approach from PixArt- δ [68], where the ControlNet is applied to the first half of the DiT [71] blocks. The output of each block is added to the output of the corresponding frozen block, serving as the input to the next frozen block. The generated tactile image \mathbf{y}' satisfying the target force and target contact position is obtained from the model $\mathbf{y}' = \mathcal{D}(\mathcal{F}_c(\mathbf{z}^{(x)}, \mathbf{z}^{(c)}, \Delta\mathbf{F}))$, where $\mathcal{F}_c(\cdot)$ is the generator built upon the force-control generator with the ControlNet. We treat the contact mask $\mathbf{c} \in \mathbb{R}^{W \times H \times 1}$ as the position-control signal, and $\mathbf{z}^{(c)} = \mathcal{E}(\mathbf{c})$ is the latent representation of \mathbf{c} obtained from the autoencoder of SANA [69]. We train the model on the aligned contact masks from FeelAnyForce [33].

3.2 Data Augmentation for Downstream Tasks

After training our two-stage conditional tactile generation framework, we apply the generated tactile images for data augmentation. Broadly, the generated images support data augmentation in three settings: tasks with force labels, tasks with pose labels, and tasks where labels remain unchanged after augmentation. Specifically, we select three tasks that require both realistic and large-scale data for effective augmentation: force estimation, contact pose estimation, and object classification.

Force Estimation. In this task, we adopt the force estimation framework proposed in FeelAnyForce [33], which is based on a ViT [73] encoder pretrained on DINOv2 [74]. The framework takes tactile images as input, consisting of a regressor that predicts the 3D force vector and a decoder that reconstructs the depth image during training to enhance the learning of the tactile-force relationship.

Contact Pose Estimation. In this task, we retain the ViT [73] encoder pretrained on DINOv2 [74] from the force estimator in FeelAnyForce [33]. The regressor output is changed from the 3D force vector to the x and y coordinates of the contact center, as well as the angle of the contact object relative to the tactile sensor. Additionally, the decoder’s supervision is shifted from depth to the contact mask. Through these modifications, we obtain a pose estimator.

Object Classification. To ensure fair comparison, we use three common classifiers: a plain CNN, a ViT [73] without pretraining, and a ViT pretrained on ImageNet [75]. The classification task involves six objects: five from the FeelAnyForce dataset [33]—banana, marker, nectarine, ring, and thick cylinder—and one additional object we collected, the T-shape. Appendix F.4 shows the objects and tactile images (Fig. 11), and Appendix D provides more details on the classifiers.

4 Experiments

In this section, we evaluate our proposed framework through extensive experiments in tactile image generation, data augmentation in three downstream tasks, and three real-world experiments. We firstly evaluate the generation quality of our two-stage conditional tactile generation framework with two baselines in Sec. 4.1. Then, we perform three downstream tasks to evaluate the data augmentation capability of our framework (Sec. 4.2, 4.3, 4.4). Finally, we deploy the trained force estimator and pose estimator into three real-world experiments (Sec. 4.5).

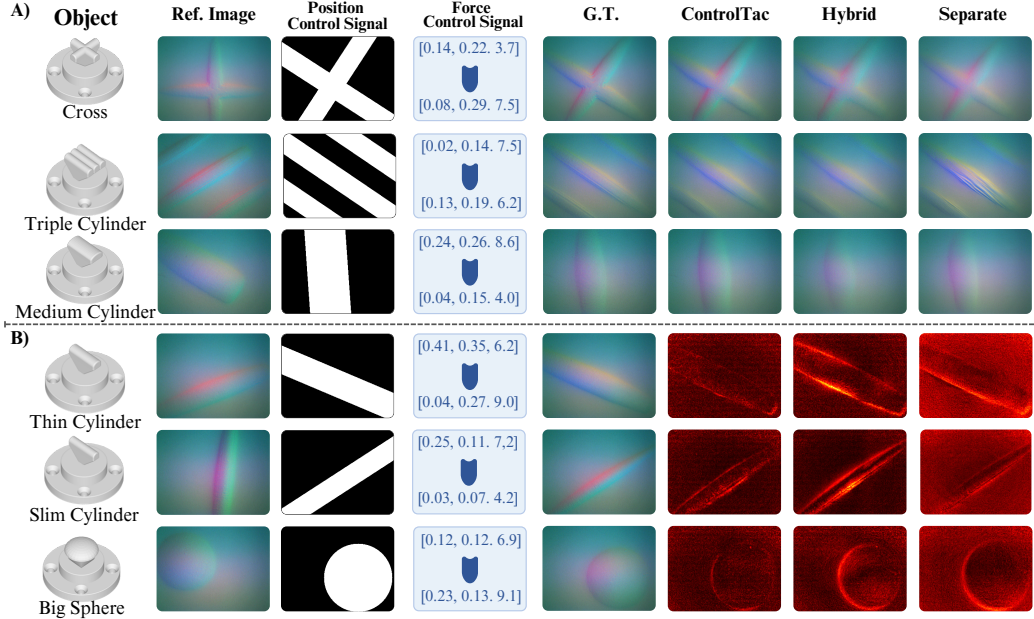


Figure 4: **Qualitative Generation Results.** The first column displays 3D previews of six objects, followed by the input tactile image (Ref. Image) in the second column and the Contact Mask in the third column. The fourth column shows the initial force (top) and target force (bottom). Subsequent columns depict the Ground Truth (G.T.) and results from CONTROLTAC, the hybrid force-position conditional diffusion model (Hybrid), and the separate-control pipeline (Separate). In part A), we visualize the generated images for comparison; in part B), we visualize the error maps highlighting the differences from the ground-truth tactile image. Complete results and force-only generation results are shown in Fig. 9 and Fig. 10 respectively in Appendix F.

We train the force-control generator component using 20,000 tactile images with corresponding 3D force vectors from FeelAnyForce [33]. The ControlNet for position-control generation is trained using 7,000 tactile images, where each object contributes 300 unique contact positions, also paired with 3D force vectors from FeelAnyForce [33]. More training details are shown in Appendix A.1.

4.1 Generation Quality Evaluation

In this section, we compare the generation quality of our two-stage conditional tactile generation framework with three baselines: (1) a hybrid force-position conditional diffusion model, which trains conditional diffusion with both force and position at the same time; (2) a separate-control pipeline, which trains the position-control using the generated images from the pretrained force-control (in the first stage) model as input; (3) the first stage of CONTROLTAC, which performs augmentation conditioned only on force. For training data, 7,000 samples are used to train the hybrid force-position conditional diffusion model. For the separate-control pipeline, we use 20,000 samples to train the force-control generator and 7,000 samples to train the position-control generator. Details of the baselines and training procedures for the three models can be found in Appendix B.

Key Findings. From Table 1, we can see that our method outperforms all baselines in both MSE and SSIM. For SSIM, it indicates that CONTROLTAC performs slightly better than the other baselines in terms of structure, gel deformation, and brightness information. For the MSE, which highlights the pixel-level difference and the generation precision, CONTROLTAC clearly outperforms the other baselines. Compared to our single-stage force-control model, our two-stage conditional tactile generation framework achieves comparable performance while enabling additional control over contact position. For the hybrid framework, the lower performance is mainly due to that force control requires more data than position control. As a result, using ControlNet [21] to finetune the pre-trained force control generator on a small amount of position data yields better performance.

Evaluation. To compare the quality of tactile images generated by CONTROLTAC with two other baseline methods and the first stage force-control generation, we calculate SSIM (Structural Similarity) and pixel-wise MSE (Mean Squared Error) on the test data of real tactile images. The test data, which comes from FeelAnyForce [33], includes the same objects as the training set but with different contact positions and forces. In Table 1, we present a comparison of SSIM and MSE for four methods; in Fig. 4, we show tactile images generated by these methods.

Table 1: Comparison in MSE and SSIM. Hybrid represents Hybrid Force-Position Conditional Diffusion Model, and Separate represents Separate-Control Pipeline.

Method	MSE ↓	SSIM ↑
Hybrid	31	0.81
Separate	157	0.79
Ours (First Stage)	18	0.84
Ours	23	0.83

In the separate-control pipeline, errors from the force-control generator and the position-control generator accumulate, leading to significantly worse overall performance.

4.2 Downstream Task: Force Estimation

In this section, to demonstrate that CONTROLTAC can generate realistic tactile images corresponding to the target force, we validate it by training a force estimator using the generated tactile images.

We first evaluate the effectiveness of the force-control generator in CONTROLTAC by comparing the performance of force estimators trained on various combinations of real and generated data. We use 1,000 different contact positions from the dataset as the real dataset and augment 20 or 40 forces with the force-control generator, resulting in datasets of 20,000 and 40,000 generated samples, respectively. We then evaluate the performance by co-training on varying amounts of real data (from 1,000 real data to 20,000 real samples) combined with the augmented data.

As shown in Fig. 5, augmenting the real data (1,000 samples) with a larger amount of generated data significantly reduces the MAE compared to using the real data alone. Moreover, with the generated dataset, the model achieves the same performance as training on the full real dataset (20,000 images) with only 8,000 real images. This suggests that the generated data effectively enrich the force distribution at each contact position, enhancing the training of the force estimator. Furthermore, combining larger quantities of both real and generated data yields the best performance, which further highlights the realism and utility of the generated data.

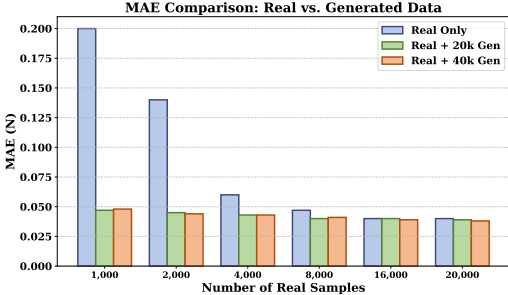


Figure 5: Force estimation performance (MAE) across different quantities of real and generated data. The normal force range is 1–10 N.

After validating the force-control generator in CONTROLTAC, we evaluate the full framework. We find that after training the second stage with ControlNet, the model becomes more sensitive to small forces. Thus, we restrict evaluation to the 4–10 N range, which reduces the real dataset from 20,000 to 15,000 samples. Under this setting, CONTROLTAC generates 15,000 or 30,000 tactile images with 750 different positions. We evaluate the performance by adding those augmented images to different number of real data for co-training (from 1,000 real samples to 15,000 real samples).

4.3 Downstream Task: Pose Estimation

In this section, to demonstrate that CONTROLTAC can generate tactile images aligned with the target contact position, we train a pose estimator using the tactile images generated by CONTROLTAC. To evaluate the performance, we train three separate pose estimators for three distinct shapes: cross, three cylinders with different curvatures and widths, and unseen T-shape.

For training the pose estimators, we use a single reference image to generate 30,000 images for each object (5,000 positions and 6 forces). We randomly sample varying number of tactile images from the generated dataset and find that the performance peaks when using 4,000 image per object. For

To demonstrate that training a high-performance force estimator requires covering different contact positions, we divided the real data according to the angles because the color of tactile images varies across different contact angles. Visualization of different angles can be found in Fig. 4 and Appendix F.1. As shown in Fig. 6, we report the MAE of force estimation under various training data settings. Incorporating position-control generation helps mitigate the challenges from limited angular coverage in the real data and significantly improves performance even with a small subset of real data, especially when the real data covers only a limited range of angles. In Appendix C, we add more experiments and analysis to the force estimations.

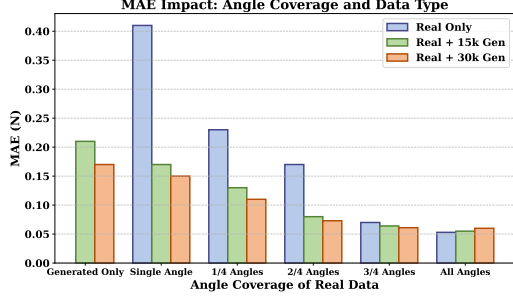


Figure 6: Force estimation performance (MAE) with different data. The sample sizes of 750, 3,750, 7,500, 11,250, and 15,000 are shown as 1, 1/4, 2/4, 3/4, and 4/4 of the contact angles.

the real tactile dataset, each object only has 300 unique contact positions, and we randomly select 3-4 forces per position to build a dataset with 1,000 samples for each object. For the unseen T-shape object, only generated tactile images are used for evaluation. In the test set, each of the three cylinder types and the cross are annotated with 30 contact positions across multiple force levels from the FeelAnyForce [33] dataset. For the T-shape, we collect 30 contact positions at a single force level.

As shown in Table 2, pose estimators trained on tactile images generated by CONTROLTAC achieves strong performance across all objects, including the unseen T Shape. In particular, using a larger amount of generated data leads to better results than using real data alone, as it is sufficiently realistic and covers a much wider range of contact positions and forces. We also compare the performance of the pose estimator using varying forces versus a fixed force (denoted as fixed in Table 2, where the fixed force is set to the median value of 6.5 N). The results show that using varying force yields better performance, as contact force naturally changes during inference.

To highlight our contribution, previous data augmentation methods using sim-and-real co-training [11] for pose estimation rely on large real datasets to achieve good performance. However, when the real dataset is reduced—e.g., to only half of its original size—the addition of large amounts

Table 2: Pose estimation errors (in pixels and degrees) under different settings.

Training Set	X ↓	Y ↓	Angle ↓
<i>Cylinder (3 Types)</i>			
3,000 real	9	8	4
3,000 gen (fixed)	13	13	6
12,000 gen (fixed)	9	8	5
3,000 gen (unfixed)	9	9	5
12,000 gen (unfixed)	4	5	3
<i>Cross</i>			
1,000 real	7	6	2
1,000 gen (fixed)	11	13	5
4,000 gen (fixed)	7	9	4
1,000 gen (unfixed)	6	9	2
4,000 gen (unfixed)	3	5	1
<i>T-shape (Unseen)</i>			
1,000 gen (unfixed)	5	5	4
4,000 gen (unfixed)	4	5	2

of simulation data fails to match the performance achieved with the full dataset. In contrast, our model can zero-shot generate a large number of realistic tactile images from a single reference image and even surpass the performance of models trained on the full real dataset.

4.4 Downstream Task: Object Classification

To evaluate the generalizability of CONTROLTAC and compare it with other data augmentations, we conduct an unseen object classification task. Objects and tactile images are shown in Appendix 11.

In this experiment, we select one reference tactile image from each of the six objects and use CONTROLTAC to generate tactile images under varying force and contact positions. For comparison, we consider a traditional data augmentation pipeline [9, 10], which applies geometric and color-based transformations to the selected reference image. The geometric transformations include rotations (eight types at 45° intervals over 360°), flipping (vertical, horizontal, and both), scaling factors (0.8,

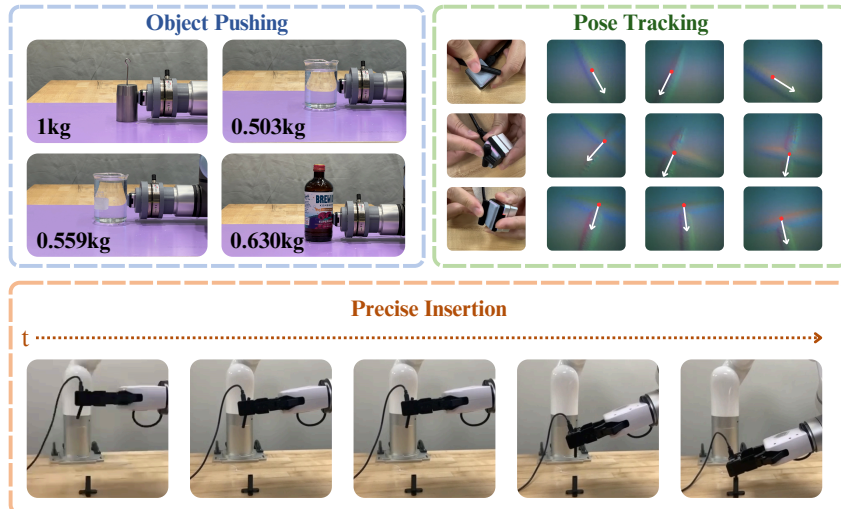


Figure 7: Qualitative examples of real-world experiments.

1.0, 1.2), and translations along two axes by $[-20, 0, 20]$, yielding 864 augmented images. The color transformations apply hue shifting to synthesis 6 color variants, resulting in 5,184 augmented images.

We evaluate classification performance using three different models: a CNN, a ViT without pre-training, and a ViT with pre-training. We train the models with data samples of size 2,400 and 4,800 using three augmentation methods. The results are summarized in Table 3. Across all models and dataset sizes, CONTROLTAC consistently outperforms traditional augmentation methods, with especially notable improvements in the ViT-based models. This demonstrates the superior utility of conditional tactile generation in enhancing downstream classification performance.

Table 3: Accuracy comparisons across models and augmentation methods. G: geometric data augmentation; C: color augmentation; Gen: our CONTROLTAC-based augmentation method.

	2400 (G)	4800 (G)	2400 (G+C)	4800 (G+C)	2400 (Gen)	4800 (Gen)
CNN	0.74	0.68	0.65	0.69	0.85	0.87
ViT (Scratch)	0.62	0.60	0.62	0.65	0.93	0.95
ViT (ImageNet)	0.78	0.76	0.74	0.79	0.99	0.99

4.5 Case Study: Real-world Experiments

In this section, we utilize the force estimator and pose estimator by training with augmented dataset in three real-world experiments: Object Pushing, Real-time Pose Tracking, and Precise Insertion.

Object Pushing. In this experiment, we estimate the pushing force between the robot and four different objects: a 1 kg calibration weight made of metal, a caliber cylinder full of water (0.559 kg) or almost full (0.503 kg), and a glass bottle of 0.63 kg. We utilize a UR5 robot with a ATI Axia80 force sensor to collect the ground truth forces for pushing. Five pushes of approximately 15s each per object are conducted at a low velocity. The overall experiment setting is shown in Fig. 7.

For evaluation, we compare our model trained on dataset augmented by the force-control generator with the model trained on the real data. As shown in Table 4, the key finding is that the force estimator trained using generated images also reaches similar performance to force estimator trained with the real dataset, which highlights that the force estimator trained with generated data generalizes well to more complex real-world scenarios and new objects with various textures, materials, and weights.

Real-time Pose Tracking. To evaluate the performance of our pose estimator, we conduct a real-time pose tracking experiment. Specifically, we press the printed cylinder, cross, and T-shape object

Table 4: Results of object pushing experiments for the four objects.

Force [N]	Weight (1.00)	Cyl. (0.503)	Cyl. (0.559)	Bottle (0.630)
Force ATI (G.T.)	2.24	0.96	1.06	1.08
Force (Real Data)	2.38	1.08	1.18	1.14
Force (Ours)	2.36	1.11	1.17	1.16

into the sensor and change the object pose by rotating and translating. In this setting, our model can track the pose in real time with 10 Hz, which highlights the practicality of the model trained with our augmented data in this dynamic real-world scenario. A visualization of the task is shown in Fig. 7.

Precise Insertion. For the precise insertion task, we 3D print three different objects (a cylinder, a cross-shaped object, a T-shape object) and a hole. We utilize the XArm7 robot arm with two GelSight Mini tactile sensors to accomplish the task using our trained pose estimator. Notably, the tolerance of this precise insertion task is only 3 mm. See Fig. 7 and Appendix A.1 for more details.

To evaluate the performance of our model, we conduct 20 insertion trials for each object type. Our force estimator achieves a success rate of 90% for the cylinder and 85% for both the cross and T-shape objects. These results highlight the practicality of our augmented data, demonstrating that a model trained data augmented from a single reference image can achieve strong performance on a challenging precise insertion task with *only 3 mm of tolerance*.

5 Conclusion

We presented CONTROLTAC, a two-stage conditional tactile generation framework capable of generating realistic and diverse tactile images conditioned on varying forces and contact positions, all from a single reference tactile image. Through experiments on three downstream tasks and three real-world experiments, we demonstrate that CONTROLTAC enables effective data augmentation and performs well in practical and challenging real-world applications. While our work marks the first attempt for controllable tactile image generation, it currently does not account for many other physical parameters beyond force and position such as surface texture and material hardness. As future work, we plan to incorporate more conditions into our framework, leveraging its modular design to support richer and more physically grounded tactile image generation.

References

- [1] Rui Li and Edward H. Adelson. Sensing and recognizing surface textures using a gelsight sensor. In *2013 IEEE Conference on Computer Vision and Pattern Recognition*, pages 1241–1247, 2013.
- [2] Ruohan Gao, Yiming Dou, Hao Li, Tanmay Agarwal, Jeannette Bohg, Yunzhu Li, Li Fei-Fei, and Jiajun Wu. The objectfolder benchmark: Multisensory learning with neural and real objects. In *Proceedings of the IEEE/CVF Conference on Computer Vision and Pattern Recognition (CVPR)*, pages 17276–17286, June 2023.
- [3] Hung-Jui Huang, Michael Kaess, and Wenzhen Yuan. Normalflow: Fast, robust, and accurate contact-based object 6dof pose tracking with vision-based tactile sensors. *IEEE Robotics and Automation Letters*, pages 1–8, 2024.
- [4] Sudharshan Suresh, Haozhi Qi, Tingfan Wu, Taosha Fan, Luis Pineda, Mike Lambeta, Jitendra Malik, Mrinal Kalakrishnan, Roberto Calandra, Michael Kaess, Joseph Ortiz, and Mustafa Mukadam. Neural feels with neural fields: Visuo-tactile perception for in-hand manipulation. *Science Robotics*, page adl0628, 2024.
- [5] Aiden Swann, Matthew Strong, Won Kyung Do, Gadiel Sznaier Camps, Mac Schwager, and Monroe Kennedy. Touch-gs: Visual-tactile supervised 3d gaussian splatting. In *2024 IEEE/RSJ International Conference on Intelligent Robots and Systems (IROS)*, pages 10511–10518, 2024.
- [6] Siyuan Dong, Devesh K. Jha, Diego Romeres, Sangwoon Kim, Daniel Nikovski, and Alberto Rodriguez. Tactile-rl for insertion: Generalization to objects of unknown geometry, 2021.
- [7] Hao Li, Yizhi Zhang, Junzhe Zhu, Shaoxiong Wang, Michelle A. Lee, Huazhe Xu, Edward Adelson, Li Fei-Fei, Ruohan Gao, and Jiajun Wu. See, hear, and feel: Smart sensory fusion for robotic manipulation. In *CoRL*, 2022.
- [8] Kelin Yu, Yunhai Han, Qixian Wang, Vaibhav Saxena, Danfei Xu, and Ye Zhao. Mimictouch: Leveraging multi-modal human tactile demonstrations for contact-rich manipulation. In *8th Annual Conference on Robot Learning*, 2024.
- [9] Philip Maus, Jaeseok Kim, Olivia Nocentini, Muhammad Zain Bashir, and Filippo Cavallo. The impact of data augmentation on tactile-based object classification using deep learning approach. *IEEE Sensors Journal*, 22(14):14574–14583, 2022.
- [10] Gang Yan, Jun Yuyeol, Satoshi Funabashi, Tito Pradhono Tomo, Sophon Somlor, Alexander Schmitz, and Shigeki Sugano. Geometric transformation: Tactile data augmentation for robotic learning. In *2023 IEEE International Conference on Development and Learning (ICDL)*, pages 346–353. IEEE, 2023.
- [11] Shaoxiong Wang, Mike Lambeta, Po-Wei Chou, and Roberto Calandra. Tacto: A fast, flexible, and open-source simulator for high-resolution vision-based tactile sensors. *IEEE Robotics and Automation Letters*, 7(2):3930–3937, 2022.
- [12] Zilin Si and Wenzhen Yuan. Taxim: An example-based simulation model for gelsight tactile sensors. *IEEE Robotics and Automation Letters*, 7(2):2361–2368, 2022.
- [13] Zilin Si, Gu Zhang, Qingwei Ben, Branden Romero, Zhou Xian, Chao Liu, and Chuang Gan. DIFFTACTILE: A physics-based differentiable tactile simulator for contact-rich robotic manipulation. In *The Twelfth International Conference on Learning Representations*, 2024.
- [14] Jiahang Tu, Hao Fu, Fengyu Yang, Hanbin Zhao, Chao Zhang, and Hui Qian. Texttoucher: Fine-grained text-to-touch generation. In *Proceedings of the AAAI Conference on Artificial Intelligence*, volume 39, pages 7455–7463, 2025.
- [15] Shaohong Zhong, Alessandro Albini, Oiwi Parker Jones, Perla Maiolino, and Ingmar Posner. Touching a nERF: Leveraging neural radiance fields for tactile sensory data generation. In *6th Annual Conference on Robot Learning*, 2022.

- [16] Yiming Dou, Fengyu Yang, Yi Liu, Antonio Loquercio, and Andrew Owens. Tactile-augmented radiance fields. *arXiv preprint arXiv:2405.04534*, 2024.
- [17] Fengyu Yang, Chenyang Ma, Jiacheng Zhang, Jing Zhu, Wenzhen Yuan, and Andrew Owens. Touch and go: Learning from human-collected vision and touch. In *Thirty-sixth Conference on Neural Information Processing Systems Datasets and Benchmarks Track*, 2022.
- [18] Jialiang Zhao, Yuxiang Ma, Lirui Wang, and Edward H. Adelson. Transferable tactile transformers for representation learning across diverse sensors and tasks, 2024.
- [19] Carolina Higuera, Akash Sharma, Chaithanya Krishna Bodduluri, Taosha Fan, Patrick Lancaster, Mrinal Kalakrishnan, Michael Kaess, Byron Boots, Mike Lambeta, Tingfan Wu, and Mustafa Mukadam. Sparsh: Self-supervised touch representations for vision-based tactile sensing. In *8th Annual Conference on Robot Learning*, 2024.
- [20] Harsh Gupta, Yuchen Mo, Shengmiao Jin, and Wenzhen Yuan. Sensor-invariant tactile representation. In *The Thirteenth International Conference on Learning Representations*, 2025.
- [21] Lvmin Zhang, Anyi Rao, and Maneesh Agrawala. Adding conditional control to text-to-image diffusion models, 2023.
- [22] Fengyu Yang, Chao Feng, Ziyang Chen, Hyoungseob Park, Daniel Wang, Yiming Dou, Ziyao Zeng, Xien Chen, Rit Gangopadhyay, Andrew Owens, and Alex Wong. Binding touch to everything: Learning unified multimodal tactile representations, 2024.
- [23] Yunzhu Li, Jun-Yan Zhu, Russ Tedrake, and Antonio Torralba. Connecting touch and vision via cross-modal prediction. In *The IEEE Conference on Computer Vision and Pattern Recognition (CVPR)*, June 2019.
- [24] Wenzhen Yuan, Siyuan Dong, and Edward H. Adelson. Gelsight: High-resolution robot tactile sensors for estimating geometry and force. *Sensors*, 17(12), 2017.
- [25] Ian Taylor, Siyuan Dong, and Alberto Rodriguez. Gelslim3.0: High-resolution measurement of shape, force and slip in a compact tactile-sensing finger, 2021.
- [26] Mike Lambeta, Po-Wei Chou, Stephen Tian, Brian Yang, Benjamin Maloon, Victoria Rose Most, Dave Stroud, Raymond Santos, Ahmad Byagowi, Gregg Kammerer, Dinesh Jayaraman, and Roberto Calandra. Digit: A novel design for a low-cost compact high-resolution tactile sensor with application to in-hand manipulation. *IEEE Robotics and Automation Letters*, 5(3):3838–3845, July 2020.
- [27] Changyi Lin, Han Zhang, Jikai Xu, Lei Wu, and Huazhe Xu. 9dtact: A compact vision-based tactile sensor for accurate 3d shape reconstruction and generalizable 6d force estimation. *arXiv preprint arXiv:2308.14277*, 2023.
- [28] Raunaq Bhirangi, Tess Hellebrekers, Carmel Majidi, and Abhinav Gupta. Reskin: versatile, replaceable, lasting tactile skins. In *CoRL*, 2021.
- [29] Raunaq Bhirangi, Venkatesh Pattabiraman, Enes Erciyas, Yifeng Cao, Tess Hellebrekers, and Lerrel Pinto. Anyskin: Plug-and-play skin sensing for robotic touch, 2024.
- [30] Subramanian Sundaram, Petr Kellnhofer, Yunzhu Li, Jun-Yan Zhu, Antonio Torralba, and Wojciech Matusik. Learning the signatures of the human grasp using a scalable tactile glove. *Nature*, 569(7758), 2019.
- [31] Binghao Huang, Yixuan Wang, Xinyi Yang, Yiyue Luo, and Yunzhu Li. 3d vitac: learning fine-grained manipulation with visuo-tactile sensing. In *Proceedings of Robotics: Conference on Robot Learning (CoRL)*, 2024.
- [32] Daolin Ma, Elliott Donlon, Siyuan Dong, and Alberto Rodriguez. Dense tactile force distribution estimation using gelslim and inverse fem, 2019.
- [33] Amir-Hossein Shahidzadeh, Gabriele Caddeo, Koushik Alapati, Lorenzo Natale, Cornelia Fermuller, and Yiannis Aloimonos. Feelanyforce: Estimating contact force feedback from tactile sensation for vision-based tactile sensors, 2024.

- [34] Hung-Jui Huang, Xiaofeng Guo, and Wenzhen Yuan. Understanding dynamic tactile sensing for liquid property estimation, 2022.
- [35] Wenzhen Yuan, Chenzhuo Zhu, Andrew Owens, Mandayam A. Srinivasan, and Edward H. Adelson. Shape-independent hardness estimation using deep learning and a gelsight tactile sensor. In *2017 IEEE International Conference on Robotics and Automation (ICRA)*, page 951–958. IEEE, May 2017.
- [36] Ruihan Gao, Kangle Deng, Gengshan Yang, Wenzhen Yuan, and Jun-Yan Zhu. Tactile dreamfusion: Exploiting tactile sensing for 3d generation, 2024.
- [37] Amir-Hossein Shahidzadeh, Seong Jong Yoo, Pavan Mantripragada, Chahat Deep Singh, Cornelia Fermüller, and Yiannis Aloimonos. Actexplore: Active tactile exploration on unknown objects. In *2024 IEEE International Conference on Robotics and Automation (ICRA)*, pages 3411–3418, May 2024.
- [38] Jianhua Li, Siyuan Dong, and Edward Adelson. Slip detection with combined tactile and visual information. In *2018 IEEE International Conference on Robotics and Automation (ICRA)*, pages 7772–7777, 2018.
- [39] Roberto Calandra, Andrew Owens, Dinesh Jayaraman, Justin Lin, Wenzhen Yuan, Jitendra Malik, Edward H. Adelson, and Sergey Levine. More than a feeling: Learning to grasp and regrasp using vision and touch. *IEEE Robotics and Automation Letters*, 3(4):3300–3307, October 2018.
- [40] Roberto Calandra, Andrew Owens, Manu Upadhyaya, Wenzhen Yuan, Justin Lin, Edward H. Adelson, and Sergey Levine. The feeling of success: Does touch sensing help predict grasp outcomes?, 2025.
- [41] Yunhai Han, Kelin Yu, Rahul Batra, Nathan Boyd, Chaitanya Mehta, Tuo Zhao, Yu She, Seth Hutchinson, and Ye Zhao. Learning generalizable vision-tactile robotic grasping strategy for deformable objects via transformer. *IEEE/ASME Transactions on Mechatronics*, 30(1):554–566, 2025.
- [42] Haozhi Qi, Brent Yi, Sudharshan Suresh, Mike Lambeta, Yi Ma, Roberto Calandra, and Jitendra Malik. General in-hand object rotation with vision and touch. In *7th Annual Conference on Robot Learning*, 2023.
- [43] Siyuan Dong and Alberto Rodriguez. Tactile-based insertion for dense box-packing, 2019.
- [44] Bo Ai, Stephen Tian, Haochen Shi, Yixuan Wang, Cheston Tan, Yunzhu Li, and Jiajun Wu. Robopack: Learning tactile-informed dynamics models for dense packing, 2024.
- [45] Ruohan Gao, Yen-Yu Chang, Shivani Mall, Li Fei-Fei, and Jiajun Wu. Objectfolder: A dataset of objects with implicit visual, auditory, and tactile representations. In *CoRL*, 2021.
- [46] Ruohan Gao*, Zilin Si*, Yen-Yu Chang*, Samuel Clarke, Jeannette Bohg, Li Fei-Fei, Wenzhen Yuan, and Jiajun Wu. Objectfolder 2.0: A multisensory object dataset for sim2real transfer. In *Conference on Computer Vision and Pattern Recognition (CVPR)*, 2022.
- [47] Arpit Agarwal, Tim Man, and Wenzhen Yuan. Simulation of vision-based tactile sensors using physics based rendering, 2021.
- [48] Ruoxuan Feng, Jiangyu Hu, Wenke Xia, Tianci Gao, Ao Shen, Yuhao Sun, Bin Fang, and Di Hu. Anytouch: Learning unified static-dynamic representation across multiple visuo-tactile sensors. In *The Thirteenth International Conference on Learning Representations*, 2025.
- [49] Carolina Higuera, Byron Boots, and Mustafa Mukadam. Learning to read braille: Bridging the tactile reality gap with diffusion models, 2023.
- [50] Fengyu Yang, Jiacheng Zhang, and Andrew Owens. Generating visual scenes from touch. *International Conference on Computer Vision (ICCV)*, 2023.
- [51] Samanta Rodriguez, Yiming Dou, Miquel Oller, Andrew Owens, and Nima Fazeli. Touch2touch: Cross-modal tactile generation for object manipulation, 2024.

- [52] Scott Reed, Zeynep Akata, Xinchun Yan, Lajanugen Logeswaran, Bernt Schiele, and Honglak Lee. Generative adversarial text to image synthesis. In *International conference on machine learning*, pages 1060–1069. PMLR, 2016.
- [53] Phillip Isola, Jun-Yan Zhu, Tinghui Zhou, and Alexei A Efros. Image-to-image translation with conditional adversarial networks. In *Proceedings of the IEEE conference on computer vision and pattern recognition*, pages 1125–1134, 2017.
- [54] Jun-Yan Zhu, Taesung Park, Phillip Isola, and Alexei A Efros. Unpaired image-to-image translation using cycle-consistent adversarial networks. In *Proceedings of the IEEE international conference on computer vision*, pages 2223–2232, 2017.
- [55] Jianmin Bao, Dong Chen, Fang Wen, Houqiang Li, and Gang Hua. Cvae-gan: fine-grained image generation through asymmetric training. In *Proceedings of the IEEE international conference on computer vision*, pages 2745–2754, 2017.
- [56] Luan Tran, Xi Yin, and Xiaoming Liu. Disentangled representation learning gan for pose-invariant face recognition. In *Proceedings of the IEEE conference on computer vision and pattern recognition*, pages 1415–1424, 2017.
- [57] Xinchun Yan, Jimei Yang, Kihyuk Sohn, and Honglak Lee. Attribute2image: Conditional image generation from visual attributes. In *Computer Vision—ECCV 2016: 14th European Conference, Amsterdam, The Netherlands, October 11–14, 2016, Proceedings, Part IV 14*, pages 776–791. Springer, 2016.
- [58] Mehdi Mirza and Simon Osindero. Conditional generative adversarial nets. *arXiv preprint arXiv:1411.1784*, 2014.
- [59] Kihyuk Sohn, Honglak Lee, and Xinchun Yan. Learning structured output representation using deep conditional generative models. *Advances in neural information processing systems*, 28, 2015.
- [60] Tero Karras, Timo Aila, Samuli Laine, and Jaakko Lehtinen. Progressive growing of gans for improved quality, stability, and variation. *arXiv preprint arXiv:1710.10196*, 2017.
- [61] Ethan Fetaya, Jörn-Henrik Jacobsen, Will Grathwohl, and Richard Zemel. Understanding the limitations of conditional generative models. *arXiv preprint arXiv:1906.01171*, 2019.
- [62] Abdul Jabbar, Xi Li, and Bourahla Omar. A survey on generative adversarial networks: Variants, applications, and training. *ACM Computing Surveys (CSUR)*, 54(8):1–49, 2021.
- [63] Achraf Oussidi and Azeddine Elhassouny. Deep generative models: Survey. In *2018 International conference on intelligent systems and computer vision (ISCV)*, pages 1–8. IEEE, 2018.
- [64] Jonathan Ho, Ajay Jain, and Pieter Abbeel. Denoising diffusion probabilistic models. *Advances in neural information processing systems*, 33:6840–6851, 2020.
- [65] Jiaming Song, Chenlin Meng, and Stefano Ermon. Denoising diffusion implicit models. *arXiv preprint arXiv:2010.02502*, 2020.
- [66] Yang Song, Jascha Sohl-Dickstein, Diederik P Kingma, Abhishek Kumar, Stefano Ermon, and Ben Poole. Score-based generative modeling through stochastic differential equations. *arXiv preprint arXiv:2011.13456*, 2020.
- [67] Robin Rombach, Andreas Blattmann, Dominik Lorenz, Patrick Esser, and Björn Ommer. High-resolution image synthesis with latent diffusion models. In *Proceedings of the IEEE/CVF conference on computer vision and pattern recognition*, pages 10684–10695, 2022.
- [68] Junsong Chen, Yue Wu, Simian Luo, Enze Xie, Sayak Paul, Ping Luo, Hang Zhao, and Zhenguo Li. Pixart- $\{\delta\}$: Fast and controllable image generation with latent consistency models. *arXiv preprint arXiv:2401.05252*, 2024.

- [69] Enze Xie, Junsong Chen, Junyu Chen, Han Cai, Haotian Tang, Yujun Lin, Zhekai Zhang, Muyang Li, Ligeng Zhu, Yao Lu, et al. Sana: Efficient high-resolution image synthesis with linear diffusion transformers. *arXiv preprint arXiv:2410.10629*, 2024.
- [70] Dongyu Luo, Jianyu Wu, Jing Wang, Hairun Xie, Xiangyu Yue, and Shixiang Tang. Diff-fluid: Plain diffusion models are effective predictors of flow dynamics. *arXiv preprint arXiv:2409.13665*, 2024.
- [71] William Peebles and Saining Xie. Scalable diffusion models with transformers. In *Proceedings of the IEEE/CVF international conference on computer vision*, pages 4195–4205, 2023.
- [72] John Canny. A computational approach to edge detection. *IEEE Transactions on pattern analysis and machine intelligence*, (6):679–698, 1986.
- [73] Alexey Dosovitskiy, Lucas Beyer, Alexander Kolesnikov, Dirk Weissenborn, Xiaohua Zhai, Thomas Unterthiner, Mostafa Dehghani, Matthias Minderer, Georg Heigold, Sylvain Gelly, et al. An image is worth 16x16 words: Transformers for image recognition at scale. *arXiv preprint arXiv:2010.11929*, 2020.
- [74] Maxime Oquab, Timothée Darcet, Théo Moutakanni, Huy Vo, Marc Szafraniec, Vasil Khalidov, Pierre Fernandez, Daniel Haziza, Francisco Massa, Alaaeldin El-Nouby, et al. Dinov2: Learning robust visual features without supervision. *arXiv preprint arXiv:2304.07193*, 2023.
- [75] Jia Deng, Wei Dong, Richard Socher, Li-Jia Li, Kai Li, and Li Fei-Fei. Imagenet: A large-scale hierarchical image database. In *2009 IEEE conference on computer vision and pattern recognition*, pages 248–255. Ieee, 2009.
- [76] Ilya Loshchilov and Frank Hutter. Decoupled weight decay regularization. *arXiv preprint arXiv:1711.05101*, 2017.
- [77] Ross Wightman. Pytorch image models. <https://github.com/huggingface/pytorch-image-models>, 2019.

A Appendix: Implementation Details

A.1 Training Configuration

Both force-control generation component and position-control generation component are trained using the AdamW [76] optimizer and a cosine annealing learning rate scheduler. For the force-control generator, the learning rate is annealed from an initial value of 1×10^{-4} to a final value of 1×10^{-5} . For the position-control generator, the learning rate decays from 1×10^{-5} to 1×10^{-6} . Each model is trained for 75,000 steps on a single NVIDIA RTX A5000 GPU with a batch size of 4. The loss function used for training is a weighted combination of L1 loss and mean squared error (MSE): $0.5 \times \mathcal{L}_{L1} + 0.5 \times \mathcal{L}_{MSE}$.

A.2 Metrics

We evaluate our models using several commonly used metrics, including mean squared error (MSE), L1 loss, mean absolute error (MAE), and structural similarity index measure (SSIM). Specifically, the following metrics are reported:

- **Mean Squared Error (MSE):** $MSE = \frac{1}{n} \sum_{i=1}^n (y_i - \hat{y}_i)^2$
- **L1 Loss:** $L1 = \frac{1}{n} \sum_{i=1}^n |y_i - \hat{y}_i|$
- **Mean Absolute Error (MAE):** $MAE = \frac{1}{n} \sum_{i=1}^n |y_i - \hat{y}_i|$
- **Structural Similarity Index Measure (SSIM):** $SSIM(x, y)$

B Details of Baselines

B.1 Hybrid Force-Position Conditional Diffusion Model:

In this approach, we train a diffusion model $\mathbf{y} = \mathcal{D}(\mathcal{F}_h(\mathbf{z}^{(x)}, \mathbf{z}^{(c)}, \Delta\mathbf{f}))$. Here, the latent representation of initial tactile image $\mathbf{z}^{(x)}$, contact mask $\mathbf{z}^{(c)}$, and target force change $\Delta\mathbf{f}$ are simultaneously input into the diffusion model $\mathcal{F}_h(\cdot)$, which is then passed into the autodecoder $\mathcal{D}(\cdot)$ to generate the output \mathbf{y} .

B.2 Separate Force-Position Conditional Diffusion Model:

In the first stage, we follow the previous force-control generator method by inputting the latent representation of the initial tactile image $\mathbf{z}^{(x)}$ and the target force change $\Delta\mathbf{f}$ into the force-control generator $\mathcal{F}_f(\cdot)$ to produce a latent representation of the tactile image $\mathbf{z}^{(x')} = \mathcal{F}_f(\mathbf{z}^{(x)}, \Delta\mathbf{f})$ that satisfies the target force. In the second stage, this generated latent representation $\mathbf{z}^{(x')}$, along with the latent representation of the contact mask $\mathbf{z}^{(c)}$, is input into the position-control generator $\mathcal{F}_p(\cdot)$. The output $\mathbf{z}^{(y)} = \mathcal{F}_p(\mathbf{z}^{(x')}, \mathbf{z}^{(c)})$, which satisfies both the target force and contact position, is then decoded to produce the final tactile image $\mathbf{y} = \mathcal{D}(\mathbf{z}^{(y)})$.

C Additional Experiments

C.1 Analysis of MAE Metrics in Different Normal Force Ranges

Table 5: MAE Metrics for Different Normal Force Ranges and Generated Data Sets.

Normal Force Range (N)	Generated Data Size	MAE ↓
1-10 N	15k	0.35
1-10 N	30k	0.33
4-10 N	15k	0.21
4-10 N	30k	0.17

The MAE is significantly higher in the 1-10 N range (see Table 5). This increase is primarily due to the sensitivity of tactile images to minor force variations when the normal force is below 4 N. Even small differences between two low forces can cause more drastic changes in the tactile image compared to variations at higher forces. Additionally, at low normal forces, the tactile image often lacks crucial information, such as detailed geometry of the contacted object, which adversely affects the model’s performance.

C.2 Impact of Data Composition on Model Performance

In our experiments, we observe that training the model with a combination of all-angle real data and generated data resulted in slightly worse performance compared to using only real data. This can be explained from two perspectives.

(1) First, the performance of the force estimator model is limited by its own capacity. As shown in Table 6, when we trained the model with varying amounts of real data (from 10k to 15k), we found that the MAE improvement plateaued once the data size exceeded 13k, indicating that adding more real data did not lead to significant gains. (2) Second, although the generated data is generally of high quality, it inevitably contains small errors. As the proportion of generated data increases, these errors tend to accumulate and negatively impact model training. Specifically, when training solely on different amounts of generated data, the MAE fluctuates as the data size increases, suggesting the presence of error accumulation. Similarly, when mixing real data with a large amount of generated data, model performance is somewhat degraded—for example, the MAE for 15k real + 30k generated is higher than for 15k real + 15k generated.

Nevertheless, the errors in the generated data are minor and do not cause a significant drop in overall model performance. This indicates that while excessive generated data can “dilute” the contribution of real data, it does not fundamentally compromise the results (see Table 6). Furthermore, even when using a much larger amount of generated data (45k or 60k) in combination with real data, the performance does not deteriorate excessively, alleviating concerns about the quality of the generated data.

Table 6: MAE of Force Estimator under Different Data Combinations. *Gen* refers to data generated by CONTROLTAC, while *Real* refers to force estimator trained by real data from FeelAnyForce [33].

Training Data Type	Data Size	MAE ↓
Real	10k	0.061
Real	11k	0.057
Real	12k	0.055
Real	13k	0.051
Real	14k	0.054
Real	15k	0.053
Gen	15k	0.21
Gen	30k	0.17
Gen	45k	0.18
Gen	60k	0.16
Real + Gen	15k + 15k	0.055
Real + Gen	15k + 30k	0.060
Real + Gen	15k + 45k	0.058
Real + Gen	15k + 60k	0.061

C.3 Impact of Contact Position Count on CONTROLTAC

In this section, we present the effects of training CONTROLTAC with different numbers of contact positions and using data generated by CONTROLTAC to train the force estimator. The results of our experiments are summarized in Table 7.

Table 7 indicates that as the number of contact positions increases, the MAE for models trained solely on generated data decreases. This suggests that more contact positions provide richer feature

Table 7: MAE results based on different contact position counts and data types. Gen refers to data generated by CONTROLTAC, while Real refers to force estimator trained by real data from FeelAnyForce [33].

Contact Position Count	Data Type	MAE ↓
100	30k Gen	0.272
100	30k Gen + 15k Real	0.077
200	30k Gen	0.207
200	30k Gen + 15k Real	0.067
300	30k Gen	0.174
300	30k Gen + 15k Real	0.060

information, thereby enhancing the model’s predictive capability. For instance, with 300 contact positions, the MAE drops to 0.174, a significant improvement over the 0.272 achieved with 100 positions.

Furthermore, incorporating real data results in even lower MAE values, particularly with 100 contact positions, where the MAE decreases from 0.272 to 0.077. This demonstrates the advantage of combining generated data with real data. Similarly, for 200 and 300 contact positions, the inclusion of real data leads to reduced MAE values of 0.067 and 0.060, respectively. This indicates that while generated data can effectively improve model performance, the addition of real data remains essential, especially with smaller datasets.

In summary, increasing the number of contact positions and integrating real data both significantly enhance the performance of the force estimator, suggesting avenues for further optimization in future research.

D Classifier Architectures

D.1 CNN Classifier

We design a convolutional neural network (CNN) for image classification, consisting of four convolutional blocks followed by two fully connected layers. The architecture is as follows:

- **Input:** RGB images of shape (3, 224, 224)
- **Convolutional Block 1:**
 - Conv2d: $3 \rightarrow 32$, kernel size 3×3 , stride 1, padding 1
 - BatchNorm2d
 - ReLU activation
 - MaxPool2d: 2×2
- **Convolutional Block 2:**
 - Conv2d: $32 \rightarrow 64$
 - BatchNorm2d
 - ReLU activation
 - MaxPool2d: 2×2
- **Convolutional Block 3:**
 - Conv2d: $64 \rightarrow 128$
 - BatchNorm2d
 - ReLU activation
 - MaxPool2d: 2×2
- **Convolutional Block 4:**
 - Conv2d: $128 \rightarrow 256$
 - BatchNorm2d
 - ReLU activation

- MaxPool2d: 2×2
- **Flatten Layer:** Feature map of shape (256, 14, 14) is flattened to (50176)
- **Fully Connected Layers:**
 - Linear: $50176 \rightarrow 512$
 - ReLU + Dropout ($p = 0.5$)
 - Linear: $512 \rightarrow 6$ (number of classes)

D.2 ViT Classifier

We use the Vision Transformer (ViT) architecture [73], specifically the `vit_base_patch16_224` variant implemented via the `timm` library [77]. This transformer-based model operates on image patches and employs self-attention mechanisms.

- **Patch Size:** 16×16
- **Input Resolution:** 224×224
- **Number of Patches:** 196 (i.e., 14×14 patches)
- **Transformer Encoder:**
 - Embedding dimension: 768
 - Number of transformer layers (depth): 12
 - Number of attention heads: 12
 - MLP dimension: 3072
- **Classification Head:** The original head is replaced with:
 - Linear: $768 \rightarrow 6$
- **Pretraining Settings:**
 - *ViT with Pretraining:* The model is initialized with weights pretrained on ImageNet 2012 [75], providing a strong starting point for transfer learning.
 - *ViT without Pretraining:* The model is trained from scratch using random initialization, without access to any external datasets.

E Details of Precise Insertion

For the precise insertion task, we 3D print three different objects and a hole: a (7 cm-long) cylinder with a diameter of (7 mm), a (7 cm) by (3 cm) cross-shaped object with (7 mm) diameter, a (7 cm) by (3 cm) T shape object with (7 mm) diameter, and a hole measuring (5 cm) in height and (3 cm) in depth with (10 mm) diameter. To finish the insertion task, we let the XArm7 with two Gelsight Mini grasp the object above the hole with a random angle and in-hand position and then adjust the pose and position according to the estimation result. The setting is shown in Fig. 7.

Specifically, the pose estimator first predict the object’s pose on the tactile sensor. Then, we compute the Euclidean distance from the estimated pose to the center. This distance is converted from pixel units to real-world units using a scaling factor of $1 \text{ pixel} = \frac{1}{20} \text{ mm}$. For estimation-based robotic control, the robot adjusts its end-effector by rotating along the Rx axis and translating along the y-axis based on the predicted pose, which align with the object vertically above the hole.

F Addition Visualizations

In this section, we provide additional visualizations to clarify the concepts discussed.

F.1 Visualization of Various Angles of Different Objects

In this section, we visualize the various angles of different objects. Fig. 8 provides valuable insights into how angle rotation can lead to dramatic changes in the tactile image's color distribution.

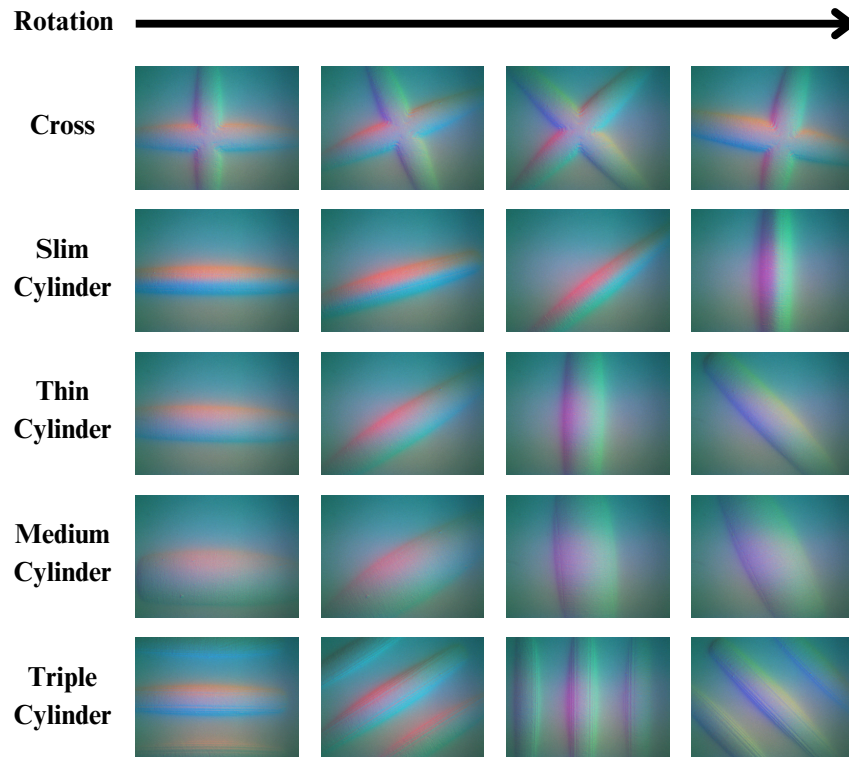


Figure 8: **Visualization of various angles.** Note: The rotational symmetry of spheres renders their angular representations redundant, and thus they are not included here.

E.2 Visualization of Error Map

In this section, Fig. 9 illustrates the error map of CONTROLTAC compared to two baseline models. It is evident that CONTROLTAC significantly outperforms the other two baseline models.

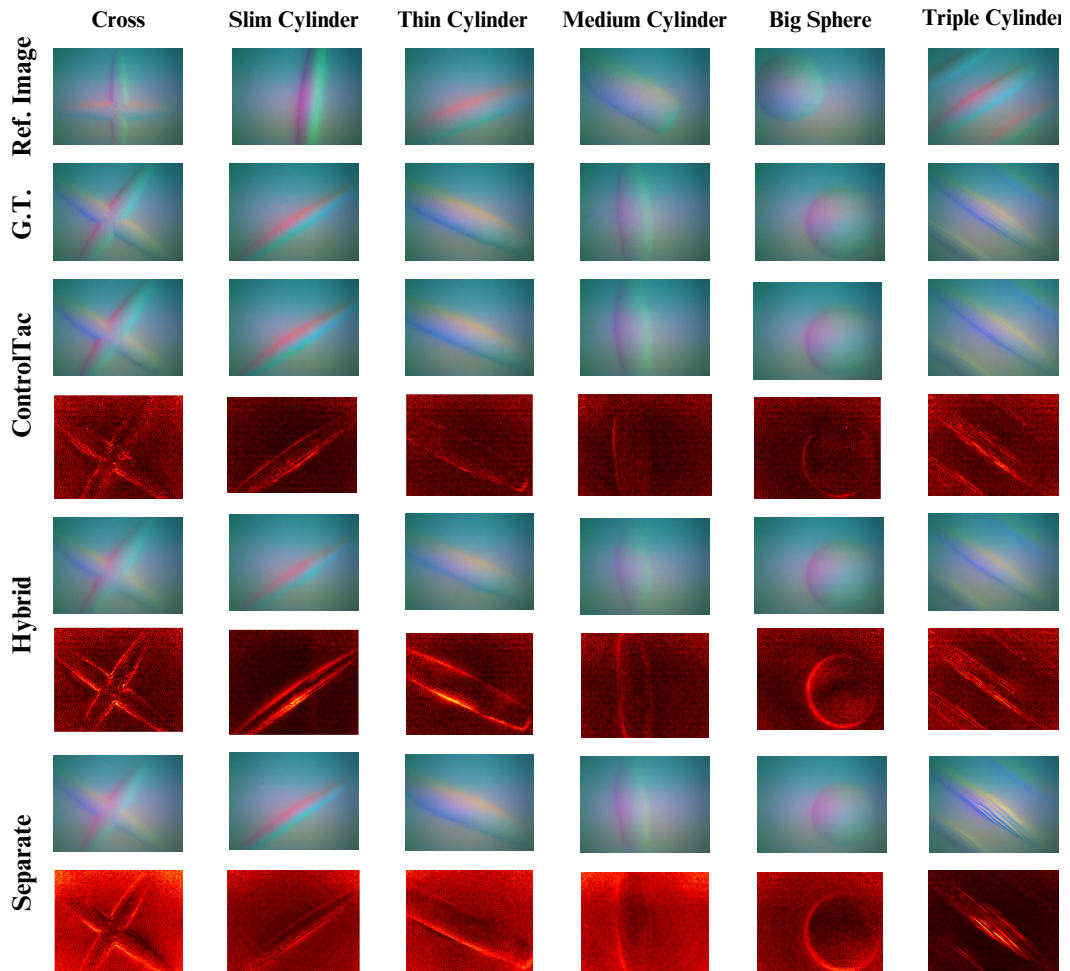


Figure 9: Error map comparison between CONTROLTAC and two baseline models.

F.3 Visualization of Generated Image using Force-Control Generation Component

In this section, we showcase the visualization results using the force-control generation component of CONTROLTAC. Fig. 10 presents the generated tactile images for the same contact position, demonstrating excellent results and the effectiveness of this component.

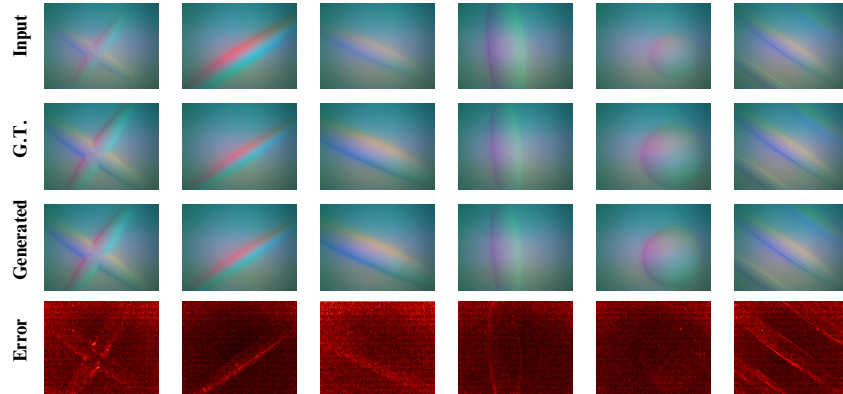


Figure 10: Generated tactile images using the force-control generation component of CONTROLTAC at the same contact position.

F.4 Object and Tactile Image Visualization for Classification

In this section, we present six objects used in the classification task along with their corresponding tactile images, as shown in Fig. 11.

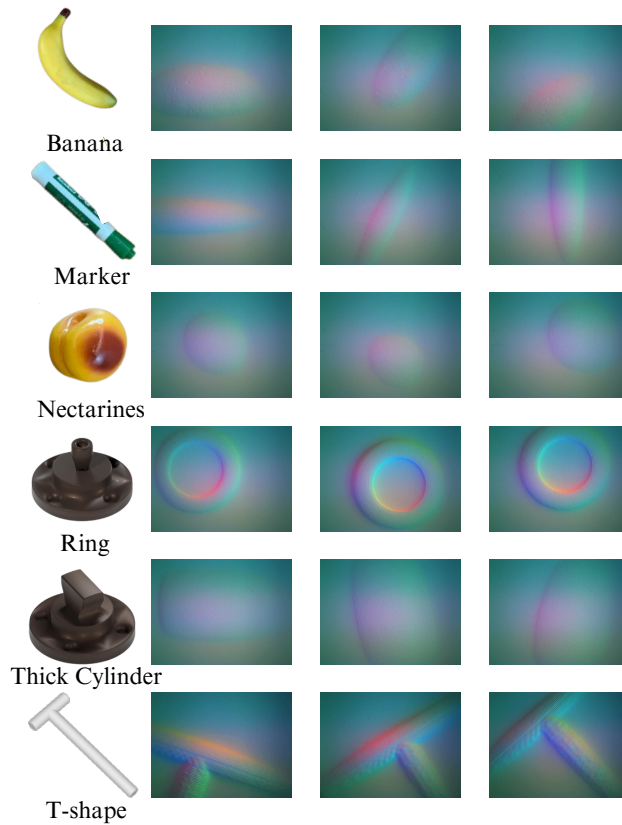


Figure 11: Six objects and their corresponding tactile images used in the classification task.